

Science

 AAAS

Determining the Dynamics of Entanglement

O. Jiménez Farías, *et al.*

Science **324**, 1414 (2009);

DOI: 10.1126/science.1171544

***The following resources related to this article are available online at
www.sciencemag.org (this information is current as of June 14, 2009):***

Updated information and services, including high-resolution figures, can be found in the online version of this article at:

<http://www.sciencemag.org/cgi/content/full/324/5933/1414>

Supporting Online Material can be found at:

<http://www.sciencemag.org/cgi/content/full/1171544/DC1>

This article **cites 16 articles**, 2 of which can be accessed for free:

<http://www.sciencemag.org/cgi/content/full/324/5933/1414#otherarticles>

This article appears in the following **subject collections**:

Physics

<http://www.sciencemag.org/cgi/collection/physics>

Information about obtaining **reprints** of this article or about obtaining **permission to reproduce this article** in whole or in part can be found at:

<http://www.sciencemag.org/about/permissions.dtl>

Despite the apparent resemblance of J1023 to 47 Tuc W and PSR J1740–5340, the latter two systems (and indeed all other currently known eclipsing pulsars with companions of several-tenths M_{\odot}) reside in globular clusters and are likely to have acquired their current companions in exchange interactions after the pulsars were “recycled” (24). J1023 is the only known highly recycled (the fifth fastest known) MSP in the field of the Galaxy with both a nondegenerate companion and an orbit that has been circularized through tidal interactions. A globular cluster origin for J1023 is extremely unlikely because of its large distance from the nearest globular cluster as well as from the Galactic bulge. The evidence points to J1023’s having been recycled by its current companion, which has not yet completed the transformation to a white dwarf.

The observed transition of J1023 suggests that it is in a bistable state: For certain rates of Roche lobe overflow, if the radio pulsar mechanism is quenched, propeller-mode accretion can occur, but if the radio pulsar mechanism is active, that same mass accretion rate cannot overcome the radiation pressure and no accretion occurs. Should the mass transfer rate of J1023 rise sufficiently, then it may enter another LMXB phase: A disk will form, the radio emission may be quenched, and the x-ray luminosity may increase dramatically, due to either propeller-mode accretion, with a net spin-down of the pulsar, or even brighter accretion onto the surface, with a net spin-up.

References and Notes

1. D. Bhattacharya, E. P. J. van den Heuvel, *Phys. Rep.* **203**, 1 (1991).
2. In a circular binary system, a star’s Roche lobe is that volume in which matter corotating with the system is gravitationally bound to that star.

3. T. M. Tauris, E. P. J. van den Heuvel, *Formation and Evolution of Compact Stellar X-ray Sources* (Cambridge Univ. Press, Cambridge, 2006), pp. 623–665.
4. L. Burderi, T. Di Salvo, F. D’Antona, N. R. Robba, V. Testa, *Astron. Astrophys.* **404**, L43 (2003).
5. J. M. Hartman *et al.*, *Astrophys. J.* **675**, 1468 (2008).
6. C. J. Deloye, C. O. Heinke, R. E. Taam, P. G. Jonker, *Mon. Not. R. Astron. Soc.* **391**, 1619 (2008).
7. J. R. Thorstensen, E. Armstrong, *Astron. J.* **130**, 759 (2005).
8. H. E. Bond, R. L. White, R. H. Becker, M. S. O’Brien, *Proc. Astron. Soc. Pac.* **114**, 1359 (2002).
9. P. Szkody *et al.*, *Astron. J.* **126**, 1499 (2003).
10. J. M. Lattimer, M. Prakash, *Science* **304**, 536 (2004).
11. R. Wijnands, M. van der Klis, *Nature* **394**, 344 (1998).
12. D. Chakrabarty, E. H. Morgan, *Nature* **394**, 346 (1998).
13. C. O. Heinke, P. G. Jonker, R. Wijnands, C. J. Deloye, R. E. Taam, *Astrophys. J.* **691**, 1035 (2009).
14. J. M. Cordes, T. J. W. Lazio, preprint available at <http://arxiv.org/abs/astro-ph/0207156> (2002).
15. I. S. Shklovskii, *Sov. Astron.* **13**, 562 (1970).
16. A. F. Fruchter, J. E. Gunn, T. R. Lauer, A. Dressler, *Nature* **334**, 686 (1988).
17. N. D’Amico *et al.*, *Astrophys. J.* **561**, L89 (2001).
18. B. W. Stappers *et al.*, *Astrophys. J.* **465**, L119 (1996).
19. S. Campana, M. Colpi, S. Mereghetti, L. Stella, M. Tavani, *Astron. Astrophys. Rev.* **8**, 279 (1998).
20. A. F. Illarionov, R. A. Sunyaev, *Astron. Astrophys.* **39**, 185 (1975).
21. L. Homer *et al.*, *Astron. J.* **131**, 562 (2006).
22. S. Bogdanov, J. E. Grindlay, M. van den Berg, *Astrophys. J.* **630**, 1029 (2005).
23. J. E. Grindlay *et al.*, *Astrophys. J.* **581**, 470 (2002).
24. F. Camilo, F. A. Rasio, in *Binary Radio Pulsars*, vol. 328 of *Astronomical Society of the Pacific Conference Series*, F. A. Rasio, I. H. Stairs, Eds. (Astronomical Society of the Pacific, San Francisco, 2005), pp. 147–170.
25. N. Zacharias *et al.*, *Bull. Am. Astron. Soc.* **36**, 1418 (2004).
26. We thank J. Condon of the NRAO for pointing out that J1023 lay within our survey beam; B. Stappers for help with WSRT observations and analysis; and S. Bogdanov, J. Thorstensen, and Z. Wang for useful discussions. The Robert C. Byrd GBT is operated by the NRAO, which is a facility of the U.S. NSF operated under cooperative agreement by Associated Universities, Inc. The Arecibo Observatory is part of the National Astronomy and Ionosphere Center, which is operated by Cornell

University under a cooperative agreement with NSF. The Parkes Observatory radio telescope is part of the Australia Telescope, which is funded by the Commonwealth of Australia for operation as a National Facility managed by CSIRO. The WSRT is operated by the Netherlands Institute for Radio Astronomy, with support from the Netherlands Foundation for Scientific Research (NWO). We thank the directors of all four facilities for their generous allocation of exploratory time to this project. ASP and GASP are collaborations funded by the Natural Sciences and Engineering Research Council of Canada (NSERC) and NSF; I.H.S. and J.v.L. thank their co-developers D. Backer, D. Nice, P. Demorest, R. Ferdman, I. Cognard, and R. Ramachandran for their hardware and/or software contributions, and P. Demorest and W. van Straten for making the PSRCHIVE software compatible with ASP/GASP data. We further thank M. Bailes, S. Kulkarni, and the others in the Caltech–Green–Bank–Swinburne–Recorder collaboration for the use of some of their computer nodes during GASP observations. J.R.B., V.I.K., D.R.L., and M.A.M. are supported by a West Virginia Experimental Program to Stimulate Competitive Research (EPSCoR) Research Challenge Grant. M.A.M. is an Alfred P. Sloan fellow. J.W.T.H. is an NWO Veni Fellow. V.M.K. is supported via the Lorne Trottier Chair in Astrophysics and Cosmology, the Canada Research Chair program, an NSERC Discovery Grant, the Fonds Québécois de la Recherche sur la Nature et les Technologies, the Canadian Institute for Advanced Research, and the Canada Foundation for Innovation (CFI). I.H.S. received support from NSERC, the CFI, the Australia Telescope National Facility Distinguished Visitor program, and the Swinburne University of Technology Visiting Distinguished Researcher Scheme.

Supporting Online Material

www.sciencemag.org/cgi/content/full/1172740/DC1
SOM Text
Fig. S1
Tables S1 and S2
References

25 February 2009; accepted 12 May 2009
Published online 21 May 2009;
10.1126/science.1172740

Include this information when citing this paper.

Determining the Dynamics of Entanglement

O. Jiménez Farías,^{1,2} C. Lombard Latune,^{1,3} S. P. Walborn,¹
L. Davidovich,¹ P. H. Souto Ribeiro^{1*}

The estimation of the entanglement of multipartite systems undergoing decoherence is important for assessing the robustness of quantum information processes. It usually requires access to the final state and its full reconstruction through quantum tomography. General dynamical laws may simplify this task. We found that when one of the parties of an initially entangled two-qubit system is subject to a noisy channel, a single universal curve describes the dynamics of entanglement for both pure and mixed states, including those for which entanglement suddenly disappears. Our result, which is experimentally demonstrated using a linear optics setup, leads to a direct and efficient determination of entanglement through the knowledge of the initial state and single-party process tomography alone, foregoing the need to reconstruct the final state.

The environment-induced dynamics of entanglement presents surprising features and challenging problems. For instance, when the parts of an entangled system interact with independent environments, entanglement may disappear at a finite time, before coherence decays (1–7). Understanding the dynamics and how it scales with the size of the system is of central

importance to quantum computing and quantum communication (8–10), as the viability of complex quantum information tasks involving many qubits (quantum bits) is intimately related to the robustness of entanglement. However, its assessment is still an open problem, especially for multipartite systems. Even for the simplest entangled systems, composed of just two qubits, subtle dynamical fea-

tures have been revealed (1, 3, 5–7). Therefore, uncovering basic dynamical laws is an appealing task that might shed some light on entanglement and the feasibility of its applications.

The marked differences between the dynamics of entanglement and the individual evolution of the components of a physical system are consequences of the nonlinear dependence of entanglement measures on the state of the system. The concurrence, for instance, introduced as a quantifier of entanglement (11), is given for a two-qubit system described by the density matrix ρ_{12} by $C = \max\{0, \Lambda\}$, where $\Lambda = \sqrt{\lambda_1} - \sqrt{\lambda_2} - \sqrt{\lambda_3} - \sqrt{\lambda_4}$. The quantities λ_i are the positive eigenvalues of the matrix $\rho_{12}(\sigma_{y1} \otimes \sigma_{y2}) \rho_{12}^* \rho(\sigma_{y1} \otimes \sigma_{y2})$ in decreasing order, where σ_{y_i} is the second Pauli matrix corresponding to qubit i and the conjugation occurs in the computational basis $\{|00\rangle, |01\rangle, |10\rangle, |11\rangle\}$. The symbol \otimes stands for the direct product of operators corre-

¹Instituto de Física, Universidade Federal do Rio de Janeiro, Caixa Postal 68528, Rio de Janeiro RJ 21941-972, Brazil. ²Instituto de Ciências Nucleares, Universidad Nacional Autónoma de México (UNAM), Apdo. Postal 70-543, México 04510 D.F. ³École Normale Supérieure, 24 rue Lhomond, 75005 Paris, France.

*To whom correspondence should be addressed. E-mail: phsr@if.ufrj.br

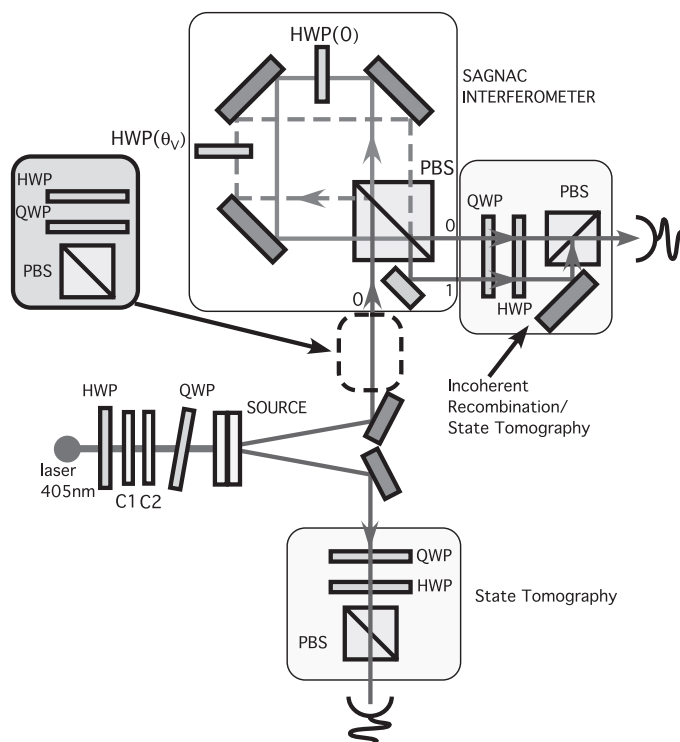
sponding to different qubits. C takes values between 0 (separable states) and 1 (maximal entanglement). The calculation of entanglement through this procedure requires knowledge of the density matrix that characterizes the system. The dynamics of entanglement is thus usually obtained from the evolved state, reconstructed through quantum tomography or calculated by considering the interaction between the entangled system and the environment, which can be represented by a “quantum channel” \mathcal{S} that transforms the initial density matrix ρ into $\mathcal{S}(\rho)$.

An alternative to these tomographic procedures that does not require the determination of the final state was recently derived (12). When one of the parts of an initially pure bipartite system interacts with a noisy environment, the evolution of entanglement can be simply described by the product of two factors that depend on the environment and the initial state, respectively. Explicitly, when a quantum channel \mathcal{S} acts on only one qubit of a two-qubit state described by the density matrix ρ , the concurrence satisfies

$$C[(I \otimes \mathcal{S})\rho] \leq C[(I \otimes \mathcal{S})|\varphi_+\rangle\langle\varphi_+|]C(\rho) \quad (1)$$

where $|\varphi_+\rangle$ is the Bell state $(|00\rangle + |11\rangle)/\sqrt{2}$. The quantity $C[(I \otimes \mathcal{S})|\varphi_+\rangle\langle\varphi_+|]$ is the concurrence of the state that evolves from $|\varphi_+\rangle$ when channel \mathcal{S} acts on the second qubit, and $C(\rho)$ is the concurrence of the initial state. The equality in Eq. 1 is valid for pure initial states. In this case, knowledge of the initial concurrence plus the characterization of the environment through its action on the state $|\varphi_+\rangle$ are enough to determine the final concurrence. If the initial state is mixed, Eq. 1 provides an upper bound for the final entanglement.

Fig. 1. Experimental setup. The elements in the gray box to the left are inserted when quantum process tomography is performed (15).



The experimental demonstration of the above equality requires (i) the production of quasi-pure quantum states, and (ii) a precise control of the quantum channel, which should act on only one of the two qubits. Both conditions are fulfilled in the experiment reported here, which leads to a clear-cut demonstration of Eq. 1. Furthermore, we show that the factorization relation in Eq. 1 can be used to estimate the entanglement of the final state through single-qubit channel tomography, which is faster and more accurate than the full reconstruction of the final state. In addition, we propose and demonstrate experimentally an extended version of the factorization relation in Eq. 1, in which the equality also applies to mixed states. We show that a universal curve describes the evolution of entanglement for arbitrary initial states.

The evolution of a density matrix under the action of a quantum channel \mathcal{S} can be written as $\mathcal{S}(\rho) = \sum_i K_i \rho K_i^\dagger$, where K_i are the Kraus operators (8). For a qubit, there can be at most four independent Kraus operators, which can be written as linear combinations of the identity and the Pauli matrices. The possible actions of the environment can then be reduced to a finite number of typical quantum channels. The set of Kraus operators completely characterizes the quantum channel. They can be obtained from the unitary evolution of the system plus environment by tracing out the environment degrees of freedom.

A paradigmatic example of a quantum channel is the amplitude channel:

$$\begin{aligned} |0\rangle_S |0\rangle_E &\rightarrow |0\rangle_S |0\rangle_E \\ |1\rangle_S |0\rangle_E &\rightarrow \sqrt{1-p} |1\rangle_S |0\rangle_E + \sqrt{p} |0\rangle_S |1\rangle_E \end{aligned} \quad (2)$$

where the subindex S denotes states of the system and the subindex E those of the environment. This equation describes, for instance, the spontaneous decay of a two-level atom interacting with a zero-temperature environment (no initial excitation in the environment). If the atom is initially in the ground state, the global state does not evolve. If the atom is excited, it has a probability p of decaying and exciting the environment. Complete decay corresponds to $p = 1$. With $p = 1 - \exp(-\Gamma t)$, where Γ is the excited-state decay rate, Eq. 2 is essentially the one derived by Weisskopf and Wigner in 1930 (13). The corresponding Kraus operators can be calculated directly from Eq. 2. We have, in this case,

$$\begin{aligned} K_1 &= \begin{pmatrix} 1 & 0 \\ 0 & \sqrt{1-p} \end{pmatrix}, K_2 = \begin{pmatrix} 0 & \sqrt{p} \\ 0 & 0 \end{pmatrix}, \\ K_3 &= K_4 = \hat{0} \end{aligned} \quad (3)$$

In our experiment, the amplitude decay channel displayed in Eq. 2 is implemented by the modified Sagnac interferometer in Fig. 1. The operation of the interferometer as a quantum channel is described in detail in (1, 3). The system states $|0\rangle_S$ and $|1\rangle_S$ correspond respectively to the horizontal (H) and the vertical (V) polarizations of a photon; the environment states correspond to different propagation modes. A single input photon is split into H and V polarization components at the polarizing beam splitter (PBS) of the Sagnac interferometer. This amounts to coupling the photon momentum and polarization degrees of freedom, as different polarizations travel in different directions after the PBS. The H component remains untouched after propagation through the half-wave plate HWP(0) inside the interferometer, while the V component propagates through a half-wave plate HWP(θ_v) that can change the polarization state. HWP(0) is used only as a path length compensator, but, depending on the setting of the HWP(θ_v), the V component is rotated. The two paths are recombined at another point of the same polarizing beam splitter. When $\theta_v = 0$, the polarization state of the field at the output in mode 0 of Fig. 1 is essentially the same as at the input. However, if $\theta_v \neq 0$, part of the V component will rotate to H and leak to mode 1. The probability that an initially V-polarized photon is flipped to H and leaks to mode 1 is $p = \sin^2 \theta_v$. This implements the quantum channel given by Eq. 2. Modes 0 and 1 are then incoherently recombined using a HWP and a PBS and sent to detection, in order to implement the experimental equivalent of performing the partial trace over the environment degrees of freedom. The final polarization state is analyzed with quantum tomography. This procedure is repeated for several values of $p = \sin^2 \theta_v$.

The initial entangled bipartite state is produced in the polarization degrees of freedom of two photons generated by spontaneous parametric down-conversion (14, 15). Quantum state tomography is performed, through an arrangement of

wave plates and PBSs (16), in order to characterize the initial state.

For each setting of p , we perform quantum process tomography (QPT) to experimentally characterize the quantum channel (15). This leads to the reconstruction of the corresponding Kraus operators (8, 17). Figure 2 shows the Kraus operators K_i ($i = 1, \dots, 4$) reconstructed from QPT measurements for different values of p . One can see that the matrix elements closely follow those in Eq. 3, implying that our setup leads to a very good implementation of the amplitude channel. The characterization of the quantum channel through QPT allows the calculation of the first factor on the right side of Eq. 1. The concurrence obtained from quantum state tomography of the final state is then compared with the one given by the factorization relation.

We study two quite different types of entanglement dynamics, corresponding to an initial quasi-pure state (for which entanglement vanishes only when $p = 1$) and to an initial highly mixed state (which leads to the vanishing of entanglement for $p < 1$). The quasi-pure state is close to $|\psi\rangle = \alpha|HH\rangle + \beta|VV\rangle$ with $\alpha \approx 0.46$, $\beta \approx 0.88$, and concurrence $C \approx 0.69$. This choice provides a more interesting scenario than a maximally entangled state, for which Eq. 1 is trivially satisfied. Mixed states are produced by letting the photon that does not interact with the environment pass through another Sagnac interferometer similar to the one in Fig. 1. The results (Fig. 3) correspond to the quasi-pure and the highly mixed state. The measured concurrence of the final state $C[(I \otimes S)\rho]$ is plotted versus the product $C(I \otimes S|\phi_{\pm}\rangle\langle\phi_{\pm}|)C[\rho]$, where $C[\rho]$ is the

measured concurrence of the initial state and $C(I \otimes S|\phi_{\pm}\rangle\langle\phi_{\pm}|)$ is obtained from the reconstruction of the channel through QPT. The different points correspond to several values of $p = \sin^2 \theta_v$, which increase in the direction of the origin ($p = 1$ corresponds to the origin in Fig. 3 where the final state becomes completely separable). Error bars were obtained from Monte Carlo simulations of experimental runs (18). Ideally, the circles indicating the quasi-pure state should stand on a linear function with a unit slope (dashed line). The linear fit of the circles has a slope of 0.87 (solid line). The slope is not exactly equal to 1 because the initial state is not perfectly pure. Mixed states lead to the inequality in Eq. 1. This is clearly demonstrated by the squares in Fig. 3, which correspond to an initial mixed state with initial concurrence $C = 0.5$ and purity 0.53. Because in Fig. 3 the parameter p of the signal interferometer increases in the direction of the origin, we note that this state leads to “sudden death” of the entanglement (1); that is, the concurrence vanishes for $p < 1$.

The characterization of the channel through QPT is made with local measurements, which are generally less demanding than the two-qubit measurements involved in bipartite quantum state tomography. Furthermore, in most real-world situations, the signal-to-noise ratio is much better for the initial state than for the final state because of unavoidable losses in the evolution process. Therefore, as compared to the full reconstruction of the bipartite state, our method provides for a more efficient determination of the final entanglement.

Our setup can be easily adjusted to implement a wide variety of channels (3), allowing, in all cases,

the characterization of the channel through QPT. In fact, this setup allows for a textbook demonstration of quantum channels (1, 3). The dashed line in Fig. 3 represents the equality in Eq. 1 and is therefore the same for all kinds of quantum channels, providing the final concurrence for initially pure states and an upper bound for initial mixed states.

It is possible, however, to extend Eq. 1 so as to always obtain the actual value of the final concurrence, irrespective of the purity of the initial state. The final concurrence is also obtained, in this generalized version, from the knowledge of the initial state and the characterization of the channel.

The basis of this result is the duality between channels and bipartite states, which implies (19, 20) that there always exists a one-qubit channel S' such that any bipartite density matrix ρ can be written as $\rho = (I \otimes S')\sigma$, where σ is a pure-state density matrix determined in the following way. The reduced density matrix corresponding to qubit 1, $\rho_1 = \text{Tr}_2(\rho)$, is written in terms of its diagonalizing basis, $\rho_1 = \sum_{i=1}^2 r_i |e_i\rangle\langle e_i|$. One then defines a pure state that yields the same reduced density matrix as the original state: $|\Psi\rangle = \sum_{i=1}^2 \sqrt{r_i} |e_i\rangle \otimes |f_i\rangle$. Then $\sigma = |\Psi\rangle\langle\Psi|$. Replacing

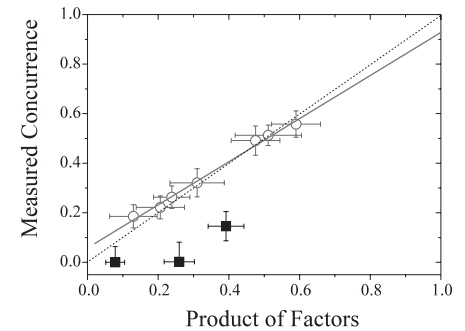


Fig. 3. Comparison between measured concurrence and the product of factors on the right side of Eq. 1. The circles and squares correspond respectively to quasi-pure and mixed initial states. The dashed line is a linear function with unit slope and the solid line is a linear fit to the circles, with slope of ~ 0.87 .

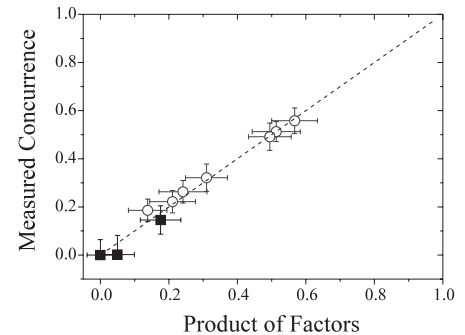


Fig. 4. Comparison between measured concurrence and the product of factors on the right side of Eq. 5. The circles and squares correspond to those displayed in Fig. 3. The dashed line is a linear function with unit slope. A linear fit to the set of all data points results in a slope of ~ 0.97 .

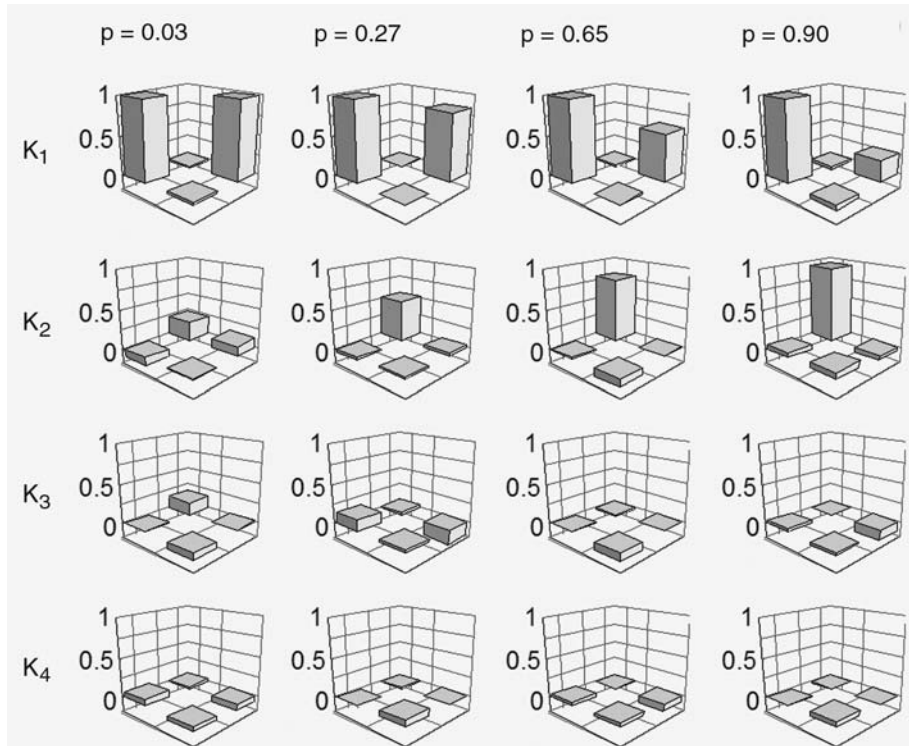


Fig. 2. Experimental Kraus operators for several values of p . Average fidelity with respect to the ideal amplitude channel given by Eq. 2 is 0.95.

this into $\rho = (I \otimes \$')\sigma$, the channel $\$'$ should satisfy the equation $\rho_1 = \sum_{i,j} \sqrt{r_i r_j} |e_i\rangle\langle e_j| \otimes \$'(|f_i\rangle\langle f_j|)$, which determines the matrix elements (indexed by a, b) of the channel $\$'$:

$$[\$' |f_i\rangle\langle f_j|]_{ab} = (r_i r_j)^{-1/2} \langle f_a | e_i \rho | e_j \rangle \langle f_b | \quad (4)$$

Because $C[(I \otimes \$)\rho] = C[(I \otimes \$')(I \otimes \$)\sigma]$, and σ is a pure state, it follows from Eq. 1 that

$$C[(I \otimes \$)\rho] = C[(I \otimes \$')|\varphi_+\rangle\langle\varphi_+|]C(\sigma) \quad (5)$$

This is the extended version of the equality in Eq. 1. It shows that even if the input state is mixed, the final concurrence is given by the product of two factors. The first factor is the concurrence of an initial Bell state evolving under the action of the product of two channels, $\$'$, acting on the second qubit, and the second factor is the concurrence of a pure state, $C(\sigma)$. Both the channel $\$'$ and $C(\sigma) = 2\sqrt{r_1 r_2}$ are obtained from the initial mixed state.

Figure 4 compares the concurrence obtained from the tomography of the final state with the product on the right side of Eq. 5, both for the

quasi-pure and the mixed states considered before. The channel $\$'$ and $C(\sigma)$ are determined from the initial state, using the procedure described above. All the points are very close to the dashed line with unit slope, which is now a universal curve for both pure and mixed states. Therefore, the benefit of obtaining the final concurrence from single-qubit QPT and the knowledge of the initial state, rather than the costlier final-state tomography, is now extended to initial mixed states.

References and Notes

- M. P. Almeida *et al.*, *Science* **316**, 579 (2007).
- L. Aolita, R. Chaves, D. Cavalcanti, A. Acín, L. Davidovich, *Phys. Rev. Lett.* **100**, 080501 (2008).
- A. Salles *et al.*, *Phys. Rev. A* **78**, 022322 (2008).
- C. Simon, J. Kempe, *Phys. Rev. A* **65**, 052327 (2002).
- T. Yu, J. H. Eberly, *Phys. Rev. Lett.* **93**, 140404 (2004).
- M. F. Santos, P. Milman, L. Davidovich, N. Zagury, *Phys. Rev. A* **73**, 040305(R) (2006).
- T. Yu, J. H. Eberly, *Science* **323**, 598 (2009).
- M. A. Nielsen, I. Chuang, *Quantum Computation and Quantum Information* (Cambridge Univ. Press, Cambridge, 2000).
- E. Knill, R. Laflamme, G. J. Milburn, *Nature* **409**, 46 (2001).
- P. Walther *et al.*, *Nature* **434**, 169 (2005).
- W. K. Wootters, *Phys. Rev. Lett.* **80**, 2245 (1998).
- T. Konrad *et al.*, *Nat. Phys.* **4**, 99 (2008).

- V. Weisskopf, E. Wigner, *Z. Phys.* **63**, 54 (1930).
- P. G. Kwiat, E. Waks, A. G. White, I. Applebaum, P. H. Eberhard, *Phys. Rev. A* **60**, R773 (1999).
- See supporting material on Science Online.
- D. V. James, P. G. Kwiat, W. J. Munro, A. G. White, *Phys. Rev. A* **64**, 052312 (2001).
- J. B. Altepeter *et al.*, *Phys. Rev. Lett.* **90**, 193601 (2003).
- J. B. Altepeter, E. R. Jeffrey, P. G. Kwiat, *Adv. At. Mol. Opt. Phys.* **52**, 107 (2005).
- A. Jamiolkowski, *Rep. Math. Phys.* **3**, 275 (1972).
- R. F. Werner, in *Quantum Information—An Introduction to Basic Theoretical Concepts and Experiments*, G. Alber *et al.*, Eds. (Springer, Berlin, 2002), pp. 14–57.
- We thank A. Buchleitner, M. Hor-Meyll, F. de Melo, and M. Tiersch for helpful discussions. Supported by a graduate fellowship from Consejo Nacional de Ciencia y Tecnología and Instituto de Ciencias Nucleares–UNAM (O.J.F.) and by the Brazilian funding agencies CNPq, CAPES, PRONEX, FUJB, and FAPERJ. This work was performed as part of the Brazilian National Institute of Science and Technology for Quantum Information.

Supporting Online Material

www.sciencemag.org/cgi/content/full/1171544/DC1
SOM Text
References

28 January 2009; accepted 16 April 2009
Published online 14 May 2009;
10.1126/science.1171544
Include this information when citing this paper.

Colloidal Nanocrystals with Molecular Metal Chalcogenide Surface Ligands

Maksym V. Kovalenko,¹ Marcus Scheele,² Dmitri V. Talapin^{1,3*}

Similar to the way that atoms bond to form molecules and crystalline structures, colloidal nanocrystals can be combined together to form larger assemblies. The properties of these structures are determined by the properties of individual nanocrystals and by their interactions. The insulating nature of organic ligands typically used in nanocrystal synthesis results in very poor interparticle coupling. We found that various molecular metal chalcogenide complexes can serve as convenient ligands for colloidal nanocrystals and nanowires. These ligands can be converted into semiconducting phases upon gentle heat treatment, generating inorganic nanocrystal solids. The utility of the inorganic ligands is demonstrated for model systems, including highly conductive arrays of gold nanocrystals capped with $\text{Sn}_2\text{S}_6^{4-}$ ions and field-effect transistors on cadmium selenide nanocrystals.

Inorganic colloidal nanocrystals (NCs) with precisely controlled compositions and morphologies have shown useful physical and chemical properties (1) and have found applications in light-emitting devices (2), photodetectors (3), solar cells (4), and other devices. Despite progress in NC synthesis, fabrication of competitive solid-state devices from solution-processed colloidal building blocks remains challenging. In a NC solid, where each individual NC carries size-dependent properties of the respective metal, semiconductor, or magnet, the transport of charges is dominated by the interparticle medium. The most

successful synthetic methodologies developed for colloidal nanomaterials use surface ligands to stabilize the particles with long (C_8 to C_{18}) hydrocarbon chains (5) or bulky organometallic molecules (6). These large molecules create highly insulating barriers around each NC. Complete removal of surface ligands has proven to be difficult and can create surface dangling bonds and charge-trapping centers (7). In a few successful examples, ligand exchange by mild chemical treatment of PbSe NC films with dilute hydrazine solutions (8, 9) or by linking CdSe NCs with 1,4-phenylenediamine (10) yielded conductive NC solids with carrier mobilities comparable to those of solution-processed organic semiconductors. At the same time, dynamic changes of volatile, easily oxidizable small linking molecules impart instabilities in the electronic properties of conductive NC solids.

It would be beneficial to design surface ligands for colloidal nanostructures that (i) adhere to

the NC surface and provide colloidal stabilization, (ii) provide stable and facile electronic communication between the NCs, and (iii) constructively supplement the properties of the NC solid. We propose a generalized approach that is compatible with existing methodology for NC synthesis and is based on exchange of the original organic ligands with molecular metal chalcogenide complexes (MCCs). MCCs provide colloidal stabilization of various nanostructures while enabling strong electronic coupling in the NC solids.

Some molecular MCCs are known as precursors for mesoporous metal chalcogenides (11–13) and semiconducting films with high carrier mobility (14, 15). Many MCCs can be synthesized by dissolution of bulk main group or transition metal chalcogenides in hydrazine (14). Excess chalcogen is usually added to form soluble anionic species such as $\text{Sn}_2\text{S}_6^{4-}$ (14) with hydrazinium (N_2H_5^+) as the counterion. Various structures including covalent (N_2H_4)₂ZnTe (16), layered $\text{N}_4\text{H}_9\text{Cu}_7\text{S}_4$ (17), and mixed-metal (N_2H_4)₅SnS₄Mn₂ (18) are accessible by this approach. Hydrazine-stabilized MCCs, whose exact molecular structure in soluble form has yet to be identified, can be prepared for many other metal chalcogenides including Ga₂Se₃, Sb₂Se₃, Sb₂Te₃, CuInSe₂, CuIn_xGa_{1-x}Se₂, and HgSe (19).

To prepare MCC-capped NCs (Fig. 1A), we developed a simple ligand-exchange procedure based on phase transfer of NCs from a nonpolar organic medium into a polar solvent such as hydrazine or dimethyl sulfoxide (DMSO) (19). Typically, a solution of MCC in anhydrous hydrazine (~1 to 5 $\mu\text{mol/ml}$) was stirred with NCs dissolved in hexane (1 to 20 mg/ml) until the organic phase turned colorless and a stable colloidal solution of NCs in hydrazine was formed. The ligand-

¹Department of Chemistry, University of Chicago, Chicago, IL 60637, USA. ²Molecular Foundry, Lawrence Berkeley National Laboratory, Berkeley, CA 94720, USA. ³Center for Nanoscale Materials, Argonne National Laboratory, Argonne, IL 60439, USA.

*To whom correspondence should be addressed. E-mail: dvtalapin@uchicago.edu